

Three-dimensional imaging of optically opaque materials using nonionizing terahertz radiation [◇]

Vincent P. Wallace,^{1,*} Emma MacPherson,² J. Axel Zeitler,³ and Caroline Reid⁴

¹*School of Electrical, Electronic and Computer Engineering, University of Western Australia, Crawley, 35 Stirling Highway, WA, 6009, Australia*

²*Department of Electronic Engineering, The Chinese University of Hong Kong, Shatin, Hong Kong*

³*Department of Chemical Engineering, University of Cambridge, Pembroke Street, Cambridge, CB2 3RA, UK*

⁴*Department of Medical Physics and Bioengineering, University College London, Malet Place Engineering Building, Gower Street, London, WC1E 6BT, UK*

*Corresponding author: vwallace@ee.uwa.edu.au

Received July 15, 2008; revised October 30, 2008; accepted October 31, 2008;
posted November 4, 2008 (Doc. ID 98734); published November 26, 2008

Terahertz electromagnetic radiation has already been shown to have a wide number of uses. We consider specific applications of terahertz time-domain imaging that are inherently three-dimensional. This paper highlights the ability of terahertz radiation to reveal subsurface information as we exploit the fact that the radiation can penetrate optically opaque materials such as clothing, cardboard, plastics, and to some extent biological tissue. Using interactive science publishing tools, we concentrate on full three-dimensional terahertz data from three specific areas of application, namely, security, pharmaceutical, and biomedical. © 2008 Optical Society of America

OCIS codes: 110.6795, 170.6920, 100.6890.

[◇] **Datasets associated with this article are available at** <http://hdl.handle.net/10376/1107>.

1. INTRODUCTION

Terahertz frequency radiation lies between the millimeter and infrared regions of the electromagnetic spectrum. The terahertz regime is typically defined as the frequency range of 0.1–10 THz [1] or, in wavelength, 3 mm to 30 μm . In this spectral region, neither optical nor electrical mechanisms of generation dominate. Sources of radiation based on interband transitions, such as semiconductor laser diodes, extend from the visible range to the mid-infrared. Beyond this, the thermal energy at room temperature and the inhomogeneous broadening of the transition states make the optical band-structure design increasingly difficult. In contrast, from the low-frequency end, power from sources based on electronic devices rolls off at frequencies above a few hundreds of gigahertz as the circuits become unresponsive. This is somewhat overcome by using frequency multipliers to obtain frequencies into the lower end of the terahertz range, which are commonly used in, for example, atmospheric research [2].

Experiments with terahertz radiation date back to measurements of black-body radiation using a bolometer by Heinrich Rubens and Fox Nichols in the 1890s [3,4]. Much later, in 1975, Auston [5] developed a photoconductive emitter gated with an optical pulse that accelerated progress toward bridging what was known as the terahertz gap. The development of stable, turn-key, ultrafast lasers was central to the development of terahertz time-domain spectroscopy and imaging techniques pioneered in the mid-1990s [6–10]. We refer the reader to a recent

comprehensive review of terahertz imaging by Chan *et al.* [11] for more background into terahertz imaging techniques, including tomography and video rate imaging, which is beyond the scope of this article.

Terahertz imaging and spectroscopy have recently been shown to have a wide range of applications in biosystems [12–14], security [15], pharmaceutical science [16], and medical imaging [17,18]. In addition to the unique spectral information in the terahertz region, which is providing new insights into crystalline structure [16,19–23], protein interactions [24,25], and explosive detection [26–28], another attractive property of terahertz radiation is its ability to penetrate optically opaque materials such as clothing, cardboard, plastics, and, to some extent, biological tissue. This paper highlights the ability of terahertz radiation to reveal information beneath or inside such materials as well as its 3-D imaging capability. Using interactive science publishing tools, we concentrate on full 3-D data from three specific areas of application, namely, security, pharmaceutical, and biomedical. This type of terahertz data is rarely seen in full 3-D due to the limitations of normal 2-D print. Before looking at the aforementioned examples, we will elaborate on terahertz pulsed imaging (TPI) in terms of the properties of the radiation, the terahertz systems used to produce it, and our methods to analyze the data.

2. TERAHERTZ PULSED IMAGING

Terahertz pulsed imaging or alternatively time-domain terahertz imaging is a noninvasive, coherent imaging

technique that can acquire inherently 3-D data. Typically, to obtain such data a terahertz beam is raster scanned across an object over two spatial dimensions (x, y) and a time-domain pulse (t) is recorded at each spatial coordinate. If the refractive index of the material under investigation is well known, then the time-domain data can be converted to a third spatial dimension (z). Another implementation using optical streak cameras has been described by Jiang *et al.* [29] that removes the need for raster scanning as a full image can be acquired in one shot.

There are many similarities between TPI and optical coherence tomography (OCT); they both provide 3-D information over a similar size scale, and they can use the same laser source for signal generation. The source is typically an ultrafast laser of which OCT utilizes the broadband output (in the near infrared) to generate high-resolution images and TPI uses the short pulses to generate broadband radiation in the terahertz frequency range, which can be used for both spectroscopy and imaging. The differences are seen when one compares wavelengths: there are several orders of magnitude between terahertz (millimeter to micrometer scale) and OCT (nanometer scale), and thus they occupy very different regions of the electromagnetic spectrum. Thus, their interactions with materials and hence sources of image contrast are very different. OCT is sensitive to the gradient of the refractive index in the near infrared, which determines scattering from structures that contain many molecules, dominated by size scales that are similar to the wavelength of light. It is also sensitive to atomic or molecular absorption, but this is generally much weaker than scattering in this part of the spectrum. OCT images are formed by the detection of light backscattered from internal structures. At terahertz frequencies the converse is true: (intermolecular) absorption is much stronger and scattering much weaker. However, in common with OCT, terahertz refractive index mismatches within materials result in strong reflections from buried layers and terahertz images are formed by the detection of absorption and refractive index changes. A typical TPI system has a usable frequency range of approximately 0.1–4 THz (3 mm to 75 μm in wavelength) with a diffraction-limited lateral resolution at 1 THz of approximately 350 μm and a bandwidth-limited axial resolution of 40 μm in air. In the simplest application, the low-coherence nature of terahertz pulses is used for time-of-flight imaging [9,30]. Reflections arise due to a change in the refractive index within the material, which, in general occurs when there is a structural or material change in the sample under investigation. The signal-to-noise ratio (SNR) associated with the technique allows small changes in refractive index to be detected and imaged. As TPI is a coherent, time-gated, low-noise technique, both phase and amplitude information can be obtained, from which the absorption and refractive index of a medium can be determined. This enables TPI to provide both structural and functional information, due to chemical specificity, enabling the investigation of both morphological and chemical changes. However, one should note that the structural and the chemical information are convolved in a single reflected or transmitted pulse and can only be separated if one is known *a priori*. In summary, the main advantages of terahertz radiation that make it a

potentially powerful technique in imaging applications are the following:

- Penetration—terahertz radiation can pass through nonmetallic and low-absorption materials such as clothing and packaging materials. It is partially reflected from interfaces between materials with different refractive indices, enabling objects made of, for example, plastic and ceramic to be detected beneath clothing. Also, terahertz radiation tends to scatter less than near-infrared and optical techniques due its longer wavelength.
- High-resolution 3-D imaging—the wavelengths used in TPI can provide images with submillimeter resolution. In addition, the extremely short pulses used in pulsed terahertz techniques enable 3-D imaging, much like radar. The range gating that this provides increases the contrast and discrimination ability beyond that given by 2-D imaging techniques.
- Spectroscopy—the broad frequency range of 10 GHz to 4 THz provides unique spectroscopic information, and many solids exhibit characteristic spectral features in this region. This enables different chemical substances to be detected, even when sealed inside an object.
- Safety—terahertz radiation is nonionizing and uses very low power levels in the nanowatt range due to the availability of high-sensitivity coherent detection schemes.

3. METHODS

Two TPI systems were used to collect the data presented in this paper, an Imaga1000 and an Imaga2000 (both from TeraView Ltd., Cambridge, UK). These time-domain imaging systems use photoconductive antennas for generation and detection of terahertz radiation and have been described elsewhere [31,32]. However, brief details are given in this paper. The major difference between the two systems is that in the Imaga1000 the near-infrared laser used for generation and detection of terahertz radiation goes through free space, whereas in the Imaga2000 it is fiber coupled.

A. Generation

In both systems, described in Subsection 3.D, terahertz radiation is generated using a photoconductive Hertzian dipole antenna gated with an ultrashort optical pulse. The antenna is produced on a gallium arsenide (GaAs) substrate, which has a bandgap of 1.42 eV, onto which gold electrodes in a bow-tie layout are patterned with a small gap in between. Optical pulses from a near-infrared (typically 800 nm) femtosecond laser focused between the gap generate free-charge carriers that accelerate across the gap when a dc bias is applied. The movement of the charge carriers and in particular their relaxation between the laser pulses results in pulses of coherent, broadband terahertz radiation being radiated from both the front and back surfaces of the antenna. The terahertz pulse is typically collected from the back surface after passing through the substrate because this is the simplest configuration to implement. However, GaAs exhibits strong absorption at these frequencies resulting in the effective bandwidth of terahertz emission limited to approximately

100 GHz to 4 THz. The central frequency, bandwidth, and pulse duration of the emitted pulse are mainly dependent on the pulse duration of the laser, the width of the antenna gap, the bandgap and lifetime of the semiconductor substrate, the bias voltage, and the thickness of the substrate. The power of the terahertz radiation generated is of the order of 100 nW and therefore well below the level of the thermal background. To detect this radiation the coherent properties of the terahertz pulses are used to distinguish them from the background. This has the advantage that the detection can be performed at room temperature and no cryogenics are needed.

B. Detection

Coherent photoconductive detection is achieved using a similar antenna to that used in emission. A second femtosecond laser beam, the so-called probe beam that is derived from the same laser used to generate the radiation, is irradiated onto the front surface of the detector. The laser pulses synchronously gate the detector, acting as a photocurrent switch by generating charge carriers. The simultaneously incoming terahertz pulse accelerates the charge carriers, and the transient current generated between the electrodes is measured by a low-current amplifier and lock-in techniques that are referenced against a modulation placed on the emitter bias voltage. The response time of the receiving antenna is determined by its gating time and the rise time of the transient photoconductivity [33]. A SNR of up to 10^6 can be achieved, which is limited by the thermal noise in the antenna.

C. Delay Line

If the path length of the pump and the probe beam are equal, the terahertz electric field is essentially measured at one instant in time. To map the whole pulse, a delay line is introduced into either the pump or probe beam, which changes the relative path length of one beam to the other. This can be performed using a mechanical translation stage that is moved at fixed intervals over a finite distance over which the entire terahertz pulse is measured. By sweeping the delay line back and forth over some distance at a particular frequency the entire pulse can be measured in fractions of a second. A number of mechanical oscillating delay lines have been suggested [34,35]. In this work a rapid-scanning delay line, oscillating at a scan rate of 15 Hz, is incorporated into the probe beam path to vary the difference in optical delay around zero between the incoming terahertz pulse and the probe laser pulse at the detector, thus allowing both the delay position and the lock-in output of the modulated external electrical field to be digitized and reinterpolated to obtain the terahertz field as a function of optical delay in real time. The reflective delay line operates at a typical frequency of 15 Hz and can be driven to approximately 100 Hz, and as a pulse can be measured over both the up and the down sweep, a pulse acquisition rate of twice this frequency can be achieved. This rate was chosen as an optimum between acquisition time and SNR. The SNR will decrease in proportion to the inverse of the square root of the scan rate, thus limiting applications where very fast data acquisition is required. By slowing the scan rate or by averaging, the SNR can be improved but with a corresponding

increase in data collection time and vice versa. The time resolution was approximately 200 fs, which is limited by the laser pulse.

D. Systems

The setup of the two systems used in this study is very similar; the portable core unit contains the ultrafast laser, optics, electronics, and computer. A 250 mW Vitesse 800 (Coherent Inc., Santa Clara, California, USA) mode-locked Ti:sapphire oscillator is used to generate and detect terahertz radiation. The 100 fs laser pulses with 800 nm central wavelength at a repetition rate of 80 MHz are split by a beam splitter into a pump and a probe beam. The probe beam is passed through the delay line as described. It is at this point that the systems deviate.

1. *Imaga1000*

The *Imaga1000* is a reflection imaging system that was used to collect most of the data in this paper. The probe beam after attenuation is focused onto the emitter. After propagating through the GaAs substrate, the terahertz pulse is collected at the back surface of the device with a high-resistivity silicon lens and then coupled into free space. The pulse is collimated by an off-axis parabolic, gold-coated mirror (OPM) and focused, with another OPM, onto the top of a 2 mm thick z-cut quartz window (see Fig. 1). Following the beam's reflection from a reference or sample placed on the quartz window, the terahertz beam is collimated and focused by another pair of OPMs onto a second high-resistivity silicon lens on the back side of the detector. The angle of reflection was 30 deg to the normal. The entire terahertz optics (indicated by the gray boxed area in Fig. 1) can be scanned, and hence the sample is mapped by the terahertz beam, by raster scanning in the x - y plane over a defined area, typically 25 mm². A complete terahertz waveform, approximately 35 ps in length, is acquired at each x - y coordinate. The signal-to-noise ratio was approximately 5000:1.

2. *Imaga2000*

The imaging of pharmaceutical tablets was performed using a TPI *Imaga2000* system. The generation of terahertz radiation in this system is based on a photoconductive switch setup as described above.

The pump and probe beams are launched into separate optical fibers that allow the terahertz radiation to be generated remotely from the TPI core unit. In this case the fibers are fed to a separate tablet scanning unit. After leaving the output from the optical fibers, the laser beams are focused onto the emitter and detector using an optical lens. The terahertz output from the emitter is coupled via a high-resistivity silicon lens into a silicon probe optic. This optic focuses the terahertz beam to a diffraction-limited spot onto a reference mirror of the tablet under investigation 5 mm away from the end of the optic. The reflected light from the tablet is collected by the same silicon optic and coupled into the detector, using a second silicon lens in contact with the rear of the detector chip. All terahertz generation and detection components together with the optics are assembled into a probe unit. The image acquisition of all surfaces of a tablet is per-

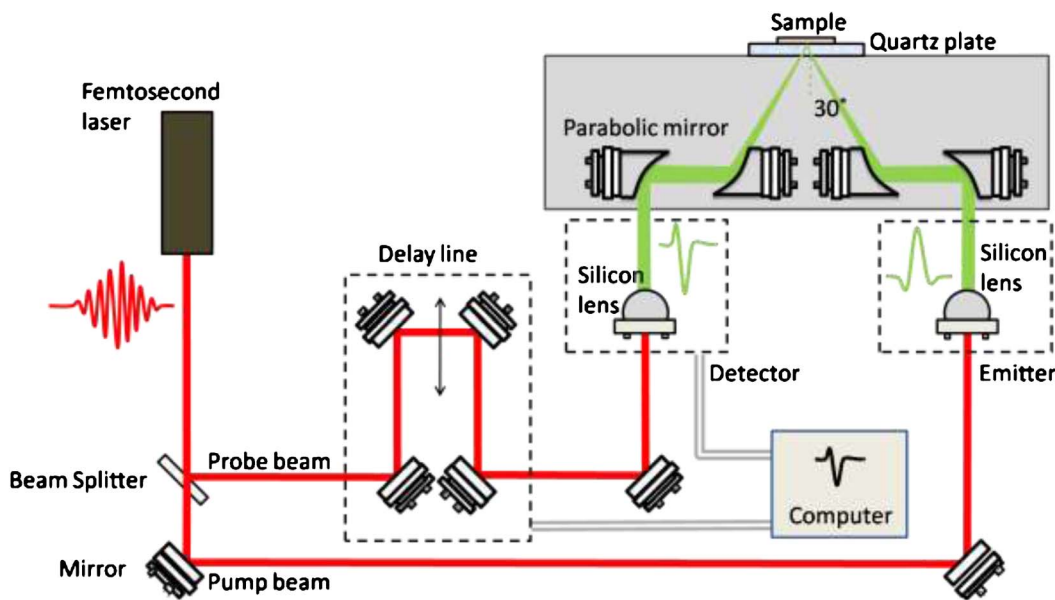


Fig. 1. (Color online) Schematic of the TPI Imaga1000 system.

formed using a fully automated six-axis robotic system (TX90, Staubli AG, Horgen, Switzerland). The robot arm adjusts the position of the sample at each point that is mapped with the terahertz pulse so that the surface at the point is perpendicular to the terahertz emitter-detector unit. The data acquisition process is therefore a two-step process: determination of the tablet shape, i.e., surface curvature, and terahertz mapping scan. The tablet shape and dimensions are determined using a laser (HeNe) scanning distance gauge. The measured profile of the tablet surface is then used to control the robot arm in front of the terahertz scanning unit and scan the tablet

across the terahertz beam until the entire surface is covered, producing a 3-D terahertz image of the tablet.

4. DATA ANALYSIS

Impulse functions are obtained from the raw terahertz reflected waveform by deconvolving the system response. The deconvolution is performed by dividing, in the frequency domain, the raw terahertz waveform reflected from the sample by a reference waveform recorded from a reference surface or just air. A numerical bandpass filter is applied to remove high- and low-frequency noise [36–38].

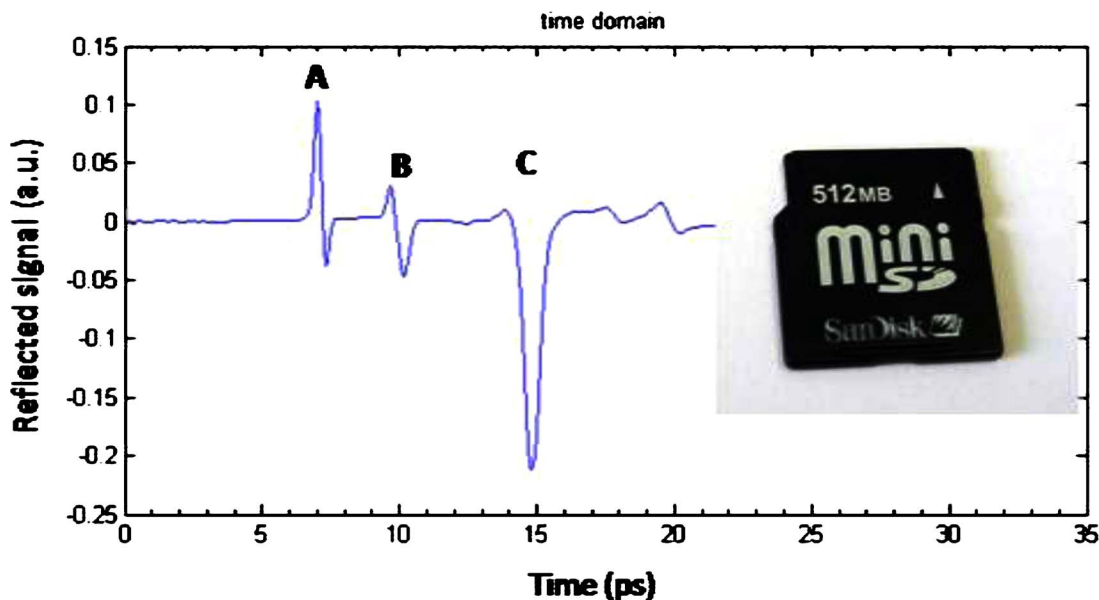


Fig. 2. (Color online) Typical deconvolved pulse reflected from the center of an SD card (inset). Three reflections can be clearly distinguished: the first peak labeled A is from the plastic surface of the card, the second peak B is a result of the terahertz beam passing through the plastic packaging and entering air, and the third negative peak is a reflection from the memory chip inside the plastic packaging.

Using this simple deconvolution process, the terahertz pulse duration of ~ 200 fs produces an axial resolution of $40 \mu\text{m}$ in air and is less within a sample as it is inversely proportional to the refractive index of the material under investigation [39].

It has been more than 10 years since the first demonstration of 3-D terahertz imaging was published by Mittleman *et al.* [40]. In that paper a 3.5" floppy disk was used to demonstrate the imaging ability of pulsed terahertz radiation. In this paper we use the example of a mini secure digital flash memory card (SD card), which typically has 700 times more capacity in approximately 0.02 times the volume. An example of typical data analysis is shown in the following figures; Fig. 2 shows an impulse function reflected from an SD Card.

Terahertz images are produced using proprietary software written in MATLAB (The MathWorks, Inc., USA). The entire terahertz 3-D dataset is read into the program. A number of methods can be employed in either the time domain or the frequency domain to display an image (see [41–43]). Plotted in Fig. 3 is the intensity at a particular peak in the time domain signal, e.g., Fig. 3(a) is obtained by plotting the intensity of the first peak seen in Fig. 2. The dimensions of the mini SD card are 21.5 mm long, 20 mm wide, and 1.4 mm thick. The plastic packaging is

approximately $250 \mu\text{m}$ thick, and internally there are two semiconductor chips on a circuit board that is $230 \mu\text{m}$ thick. The two chips [a control chip, Fig. 3(e), and the main memory chip, Fig. 3(d)] differ slightly in thickness and can be resolved from each other.

Nonstationary signals such as terahertz pulses often have relatively short-lived high-frequency features and long-lived low-frequency features; thus a suitable analysis tool is one that can resolve high-frequency content well in time and low-frequency content well in frequency [44]. Unfortunately it is not possible to resolve both time and frequency well simultaneously due to the constraints of uncertainty, and therefore a compromise must be reached. Although the Fourier transform is the standard spectral analysis technique, it performs poorly at analyzing nonstationary signals, as the frequency content is considered over the entire time-domain pulse. The short-time Fourier transform (STFT), or windowed Fourier transform, is therefore used to overcome this limitation [44,45]. The window function has fixed time and frequency resolution, however, which is still a shortcoming. Wavelet transforms are an alternative method [46,47] but have not been explored here. If the sample has a thin layered structure, in a region of the image we can use higher-frequency components to find and highlight it. Thus we

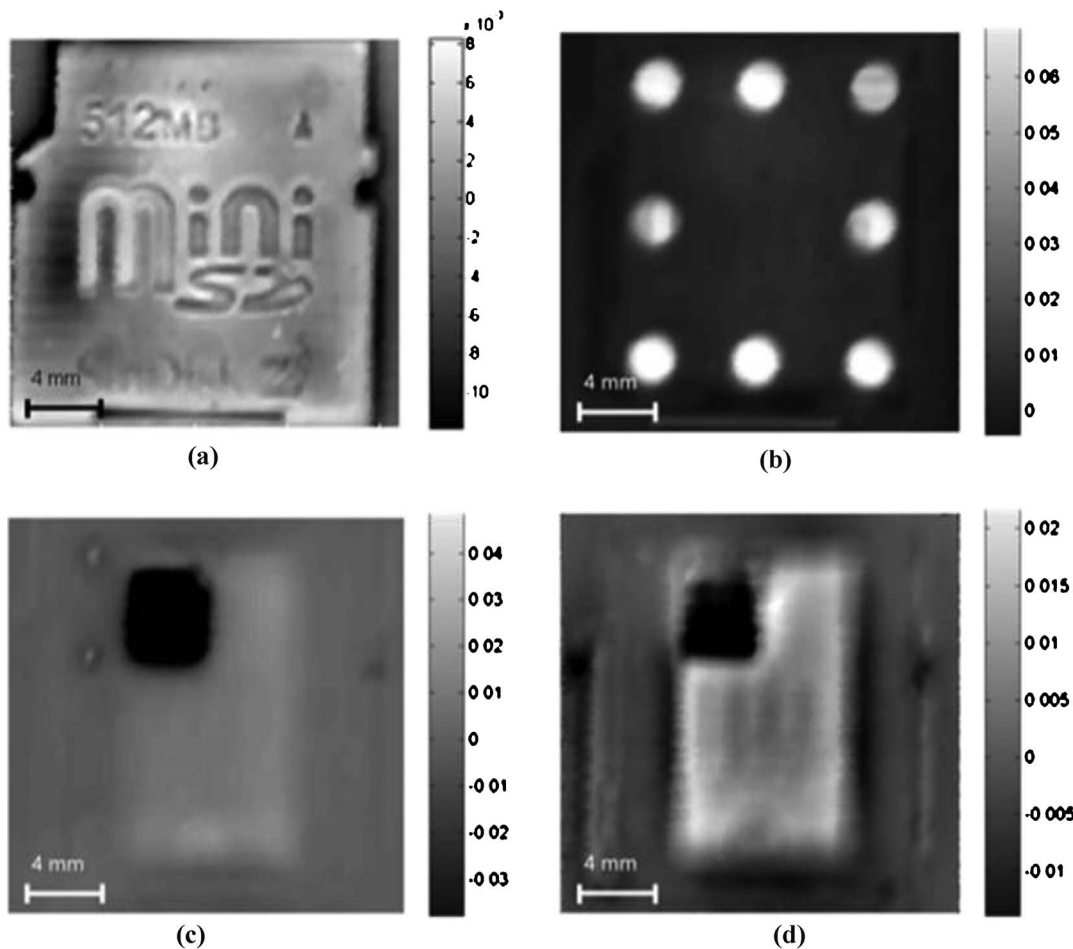


Fig. 3. Each image is a terahertz image of the SD card at different time points along the pulse. (a) Image at 10 ps along the pulse that is at the surface of the SD card. (b) Image at 11.5 ps that shows six spots where the plastic packaging is bonded together. (c) Image at 15.0 ps showing a control chip that is approximately 3 mm^2 . (d) Image at 16.7 ps that shows the main memory chip inside the SD card.

can choose a window that gives information over each layer. If the layer is too sharp, spatial information is lost. For the SD card we chose a small time window to match the thin structures to analyze the frequency components as shown in Fig. 4. The time–frequency analysis of the data from the SD card is shown in Fig. 4. Figure 4(a) is a time–frequency terahertz image at $t=21.4$ ps and $f=1.51$ THz. Around the edges you can see the back part of the packaging; the dark rectangular central area is where the memory and control chips are located. Due to their highly reflective properties, the terahertz radiation does not penetrate through them. Figure 4(b) is a time–frequency plot of a pulse taken from position pixel $x=38$ and $y=36$ on the image in Fig. 4(a). For each point in time along the x axis there is a corresponding frequency spectrum plotted along the y axis. By changing the window

width of the short time frequency transform we can resolve thin structures within the SD card. Figure 4(c) is the frequency spectrum of the time-domain pulse given in Fig. 4(d), which has been optimized by varying the time window to resolve the layers in the SD card. Finally, Figs. 4(e) and 4(f) are cross-sectional images through the card at $x=36$ and $y=38$, respectively. In Fig. 4(e) the bottom bright line is the interface between the quartz glass and the plastic packaging. The next lineup is the internal surface of the plastic packing. Then there are two more bright lines: the shorter, lower one is the reflection from the controller chip, and the next line is the reflection from the memory chip. Deeper still, between 20 and 25 ps, there is the backside of the packaging that is shown in Fig. 4(a). In Fig. 4(f) a cross section of three of the plastic pins that were shown in Fig. 3(b) can be seen (at approxi-

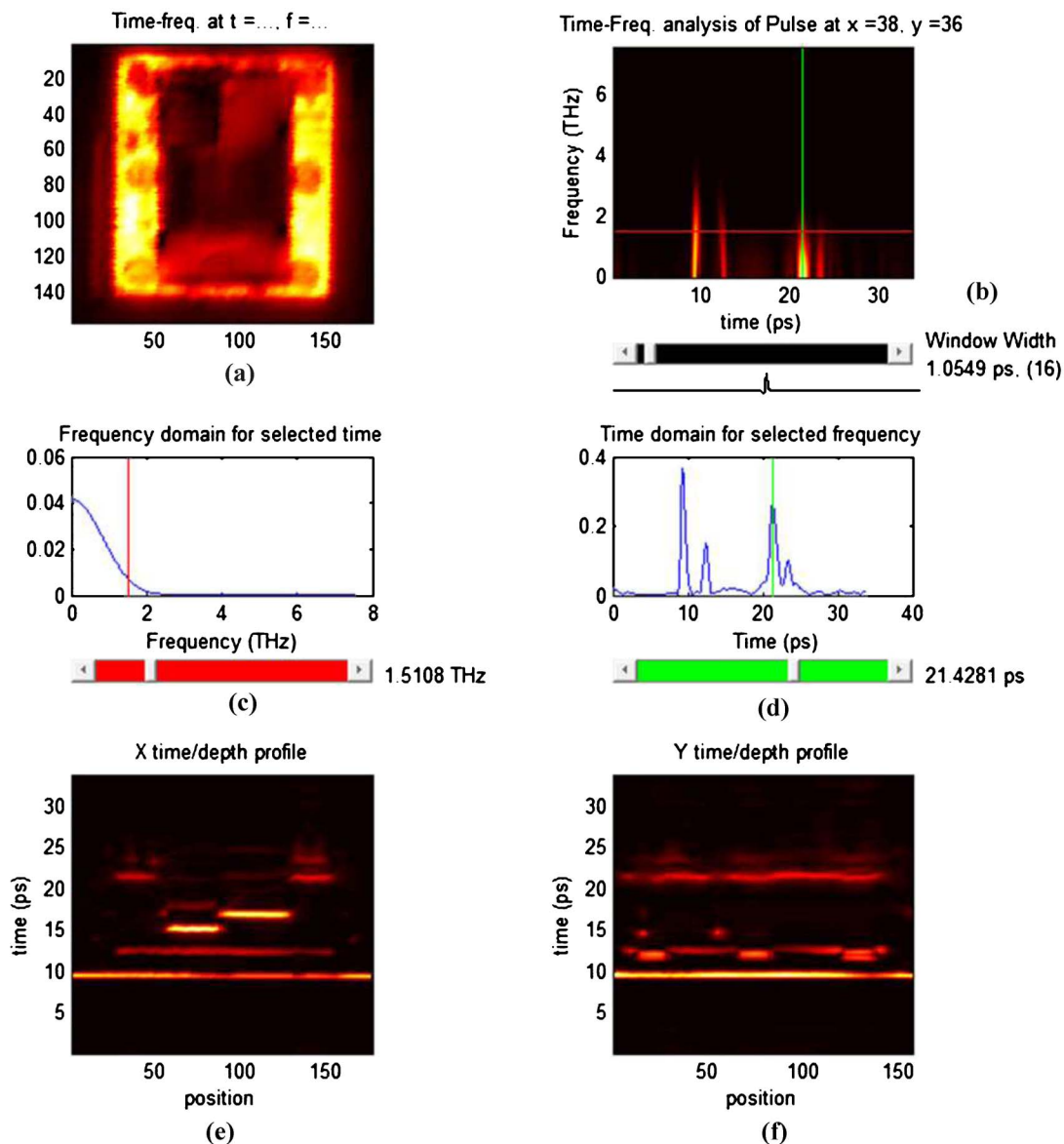


Fig. 4. (Color online) Time-frequency analysis of the data from the SD card. (a) Time-frequency terahertz image at $t=21.4$ ps and $f=1.51$ THz. (b) Time-frequency plot of a pulse taken from position pixel $x=38$ and $y=36$ (a). (c) Frequency spectrum of the time domain pulse given in (d), which has been optimized by varying the time window to resolve the layers in the SD card. Cross-sectional images through the card at (e) $x=36$ and (f) $y=38$.

mately 12 ps), as these data are taken along the length of the packaging at the side. In addition, both the front and back surfaces of the packaging of the SD card are detected.

An optimized 3-D dataset can then be saved in a specific format (in this case Visualization ToolKit or vtk) for later visualization. These data are shown in Fig. 5; as the image is rotated the layered structure is clearly visible. This example demonstrates the potential of terahertz imaging for nondestructive testing and quality control.

Having described our imaging systems and worked through an example to illustrate our processing techniques, we now show, with further 3-D terahertz datasets as examples, how terahertz imaging is being applied to problems in security, pharmaceutical, and biomedical applications.

5. SECURITY APPLICATIONS

As terahertz radiation penetrates many everyday physical barriers such as clothing and packing materials with modest attenuation it makes it a potentially powerful technique in security screening [48]. In addition, many chemical substances and explosive materials exhibit characteristic spectral responses at terahertz frequencies that can, under certain conditions, identify these objects [49]. Terahertz techniques therefore combine safe-to-use high-resolution imaging and sample identification through spectroscopy, even when samples are hidden in packaging, mail items, or under clothes.

Terahertz radiation will propagate modest distances through normal atmospheric air and can therefore be considered for stand-off detection [50]. Terahertz imaging systems can be passive, simply detecting the terahertz part of the thermal black-body radiation given off by objects; for example, the human body naturally radiates more than 1 W of power at terahertz frequencies. Alternatively, active schemes can be implemented whereby the object being imaged is illuminated by a terahertz source. Although passive systems may be effective for 2-D low-frequency (e.g., 100 GHz) millimeter-wave imaging, chemical and structural analysis of suspect objects is restricted to broadband frequency techniques, as there are virtually no spectroscopic features in solids below

500 GHz [28]. TPI can be several times more sensitive, but its implementation for security settings still remains a challenge. For instance, data acquisition times are relatively slow and there are restrictions on sample geometry due to limited penetration depth.

Enhancements in detecting weapons containing a small amount of metal, ceramic weapons, explosive materials, or chemical or biological threats are desired. Emerging imaging technologies such as those using x-ray backscatter and millimeter waves could be implemented; however, x-ray backscatter uses ionizing radiation. Furthermore, neither technique is capable of providing chemical or structural analysis of suspect objects in the image. Thus x-ray and millimeter-wave portals will result in the need for further searching whenever the image indicates a suspect item or area.

Here we present two examples of 3-D terahertz datasets relevant to security screening. The first is a ceramic knife hidden under layers of clothing and the second is a letter in an envelope.

A. Hidden Knife

The purpose of this experiment was to test the potential of TPI to detect an object hidden under multiple layers of clothing (this is the same data as presented in [48]). A ceramic knife blade was placed next to the subject's skin. The object was covered with two layers of a woolen sweater and four layers of a cotton shirt material, as depicted in Fig. 6(a). Data were taken in reflection using the TPI Imaga1000 and processed using the STFT. Figure 6(b) shows images of the ceramic blade. The image shows processed 3-D data where the red region is the ceramic blade and the different layers of clothing (blue and green) are just visible. In this case the blade can be clearly identified under several layers of clothing due to the large change in refractive index between the clothing materials and the ceramic blade.

B. Mail Screening

In this second security-related example we wrote the letters THz on a standard piece of A4 paper. The paper was then folded into three and placed inside an envelope. The letter was then scanned using the Imaga1000. Figure 7(a) shows the reflected impulse function at a single point. The first trough is the quartz-envelope boundary and the following three peaks are due to three layers of paper in the folded letter—the troughs are due to the air gaps between the paper layers. The penultimate peak is due to the envelope layer, and the last and largest peak is a reflection from a mirror placed on top of the envelope during scanning. The envelope and individual pages can be clearly resolved in the cross-sectional image shown in Fig. 7(b); from the bottom of the image, the first dark horizontal line is the quartz-envelope interface. The horizontal yellow and blue lines are the individual layers of the paper. The letters THz are written on the second layer and can be clearly seen as dips in the line at 40, 80, 100, and 120 along the x axis. Rather than resulting in a change of thickness, the letters' visibility is more likely due to an increase in absorption and/or refractive index, but since we do not know the refractive index of ink on paper we cannot convert the y axis from time into distance. Figure 8(a)

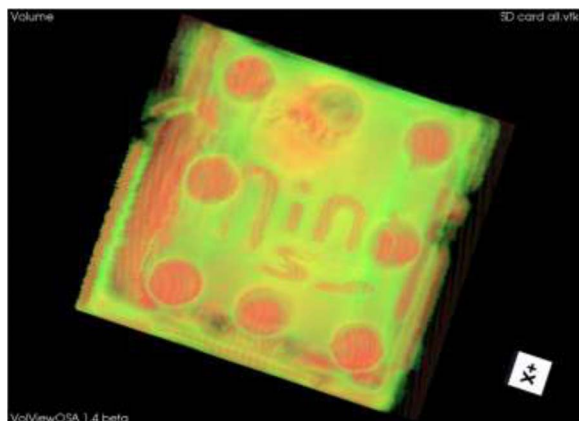


Fig. 5. (Color online) A 3-D view of the SD card (View 1).

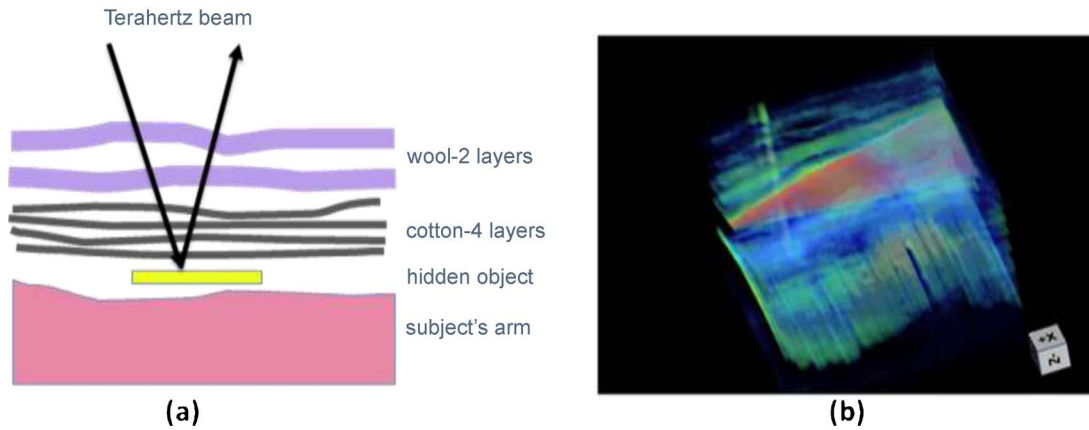


Fig. 6. (Color online) (a) Schematic of the hidden object, the ceramic blade, under several layers of clothing. (b) 3-D view (View 2) of a knife colored in red, seen under the layers of clothes shown in green and blue as they are semitransparent at terahertz frequencies.

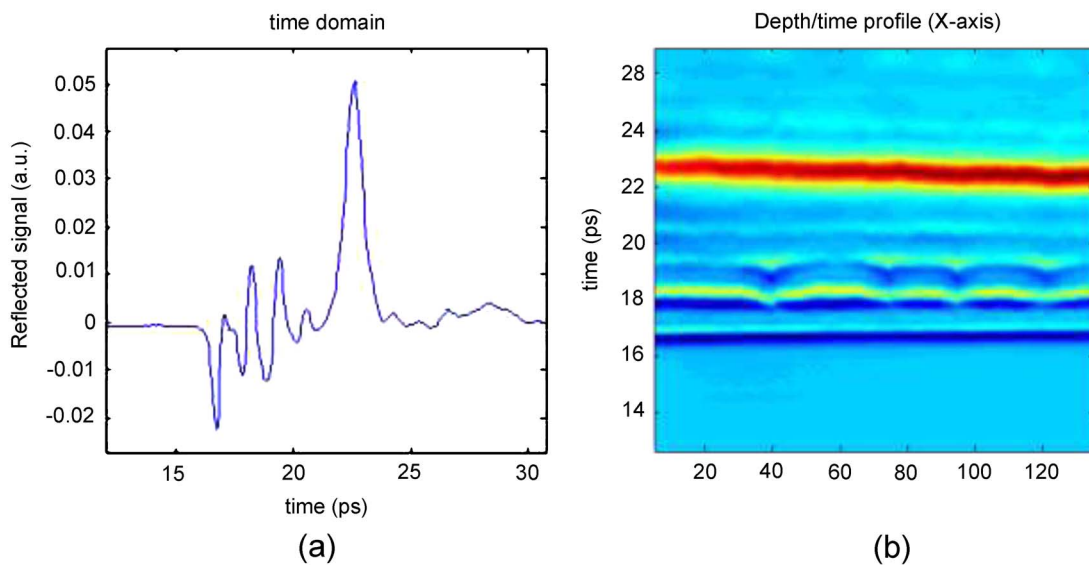


Fig. 7. (Color online) (a) Time-domain impulse function and (b) cross-sectional image from a folded letter within an envelope.

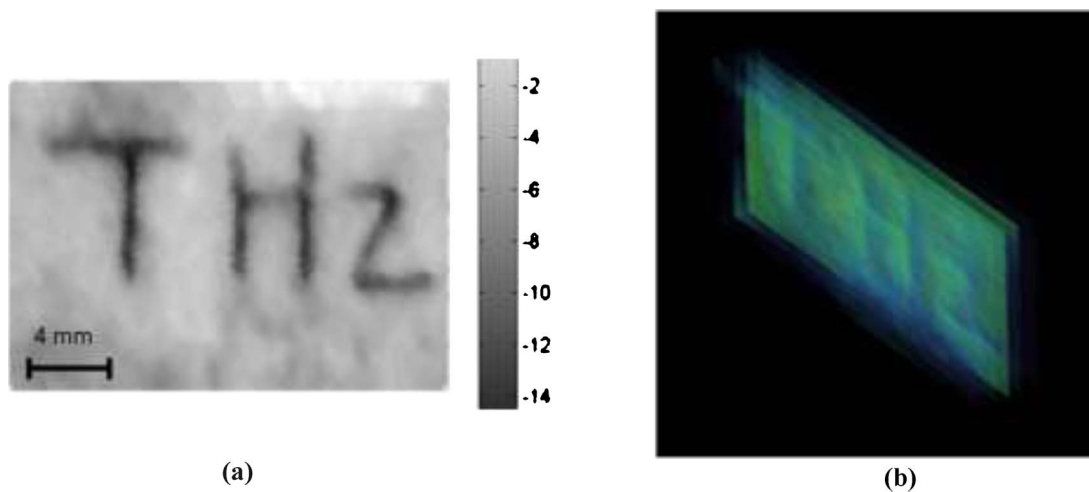


Fig. 8. (Color online) (a) Terahertz intensity image from the third layer in the envelope (approximately 19 ps) and (b) 3-D image of the letter (View 3).

shows a terahertz intensity image at 19 ps, and Fig. 8(b) shows the 3-D dataset, where you can peel away the pages to reveal the writing on the folded page inside the

envelope. This was a relatively simple setup as there was no overlapping with the writing on the other layers. The presence of the writing on a layer reduces the intensity of

the reflected peak, and the time delay shifts slightly. To look at full pages of text would be far more complicated, especially if writing was overlaid in deeper layers, but further image analysis and character recognition software could probably decipher the contents of such a letter. This simple example elegantly illustrates the power of TPI to reveal hidden information, but, due to resolution and signal-to-noise constraints, it is unlikely to be an important enough application to be developed further.

6. PHARMACEUTICAL APPLICATIONS

In modern pharmaceuticals the tablet remains the single most important solid dosage form that is used to administer drugs to a patient. It is the dosage form of choice because it combines reproducible drug dosage, high stability during storage, and can be economically produced. Conveniently, a number of techniques are available to control the release kinetics of the drug that is embedded in the tablet: coating layers can be applied that dissolve rapidly at elevated pH while being insoluble in the acidic conditions of the stomach (enteric coatings), slowly eroding polymer coatings or matrices can be used to modify the drug release rate, or tablets can even be subdivided into different segments (layered, dry-coated tablets or oral osmotic delivery systems).

The development of advanced tablets requires quality control techniques that are ideally nondestructive, give spatially resolved information, and have a strong specificity to the properties that limit the quality of the tablet once it is administered to the patient. TPI is emerging in the field and has demonstrated a strong potential to address the needs of the industry [16,51,52].

Since the first demonstration of the TPI measurement principle for the determination of the coating thickness of a sugar-coated tablet by Fitzgerald *et al.* [53], the technique has been used to perform both 2-D [54,55] and 3-D chemical imaging [56].

Commercial equipment has been developed to acquire fully automated terahertz data of all surfaces of tablets of almost any shape [31]. It can provide spatially resolved quantitative measurements of layer thickness through multiple film coating layers [57] and detect weak spots on the coating that are not visible to the naked eye; these properties affect the tablet performance [57,58].

The ability to measure quantitative density maps of a tablet using TPI was investigated by Palermo *et al.* [59]. A multivariate calibration was performed that was able to predict the density of compacted mixtures of four excipients. Using this multivariate model, the density distribution over the surface of flat tablets was predicted from the TPI maps. Obradovic *et al.* [60] demonstrated how TPI can be used to study diffusion processes into a polymer matrix, a process that is key to the characterization of sustained release matrix tablets.

Figures 9–11 are examples of TPI data used in tablet analysis, all obtained using the Imaga2000.

Figure 9 shows the internal structure of a layered tablet that is also coated with a polymer film. The overall dimensions of the tablet are approximately 1.9 cm in the x direction and approximately 0.9 cm in the y direction. The interface between the two layers of the tablet is located at

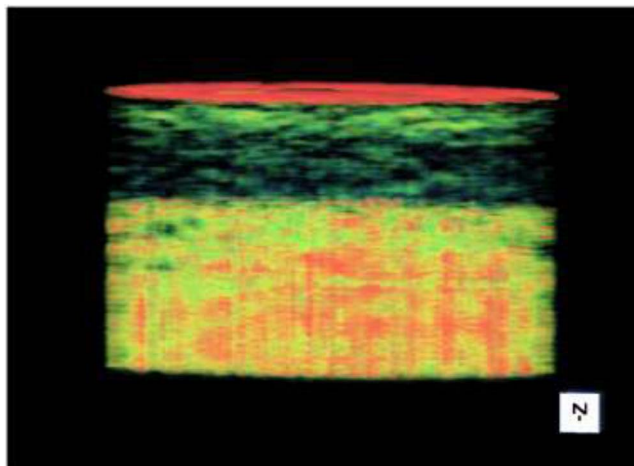


Fig. 9. (Color online) Layered tablet with a polymer film coating (View 4). The coating is clearly seen at the top of the image in red. The tablet has two layers clearly shown, the first, in this image, is virtually transparent (using these display settings), and the second layer has a different structure resulting in a strong signal shown in red/green/yellow. In reality the tablet surface is curved, but the processing software flattens the image.

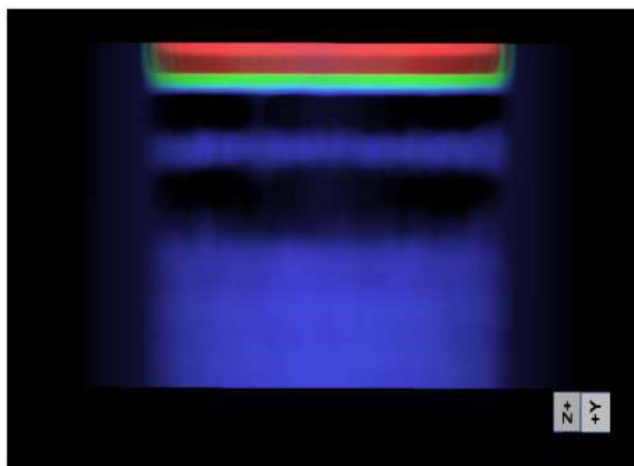


Fig. 10. (Color online) Bilayer polymer tablet (View 5).

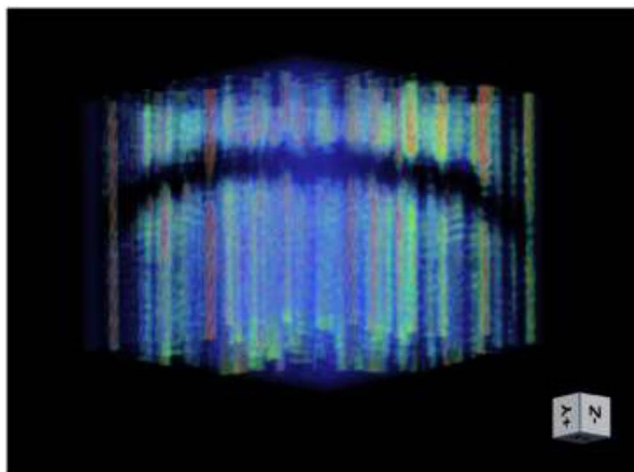


Fig. 11. (Color online) Three-dimensional image of a soft gelatin capsule (View 6).

a depth of approximately 2 mm in the z direction. In addition to this interface between the bulk layers of the tablet, a strong interface between the film coating and the tablet can be detected (the red layer). The thickness of the polymer layer is nonuniform, exhibiting a bimodal distribution around 53 and 73 μm . All structures highlighted in the figure are relative to the top surface of the tablet. Although the surfaces of all samples are curved in reality, hence the requirement for the Imaga2000 to first do a surface scan, the 3-D data show the structure of the internal features within the tablet as if the tablet surface was flattened out, as it appears to the terahertz sensor when the robot arm positions the tablet at normal incidence to the optics. The real geometry of the tablet is determined in the surface scan using a laser gauge, as previously described, before the terahertz scan, and it is possible to change the projection of the 3-D terahertz data to match the real shape of the sample as determined in the surface scan.

Figure 10 shows terahertz data acquired from a film-coated tablet with two layers of polymer coating (Tablet A in [31]). The first coating layer is approximately 42 μm thick (red) and the second layer measures approximately 67 μm in thickness (green).

The sample in Fig. 11 is a soft gelatin capsule (Capsule A in [31]). Soft gelatin capsules are produced by welding two sheets of soft gelatin together after a liquid filling has been injected between the sheets. The image highlights the seam area between the two sheets. It can be clearly seen that the gelatin sheets are of different thickness. The gap of the seam is at a depth where the TPI measurement is below the axial resolution of the instrument.

7. BIOMEDICAL APPLICATIONS

Early experiments by Hu and Nuss [8] demonstrated that terahertz imaging could have biomedical applications; their terahertz images of porcine tissue showed a contrast between muscle and fat. Since then TPI has revealed the contrast between regions of healthy skin and basal cell carcinoma (BCC) both *in vitro* [36] and *in vivo* [32]. More

recently TPI has been used to identify tumor margins on excised breast carcinoma [61]. Statistically significant differences are seen between terahertz spectroscopic measurements of normal tissues and both BCC and breast tumors [62,63]. The spectra of diseased tissue are close to that of water, and double Debye theory has been used to describe the interaction of terahertz with tissue [64–66].

Thus the advantage of TPI over other imaging techniques is its sensitivity to water. This provides a natural contrast agent for identifying cancer [65], which has been shown to contain more water than normal tissue. This also makes it a suitable tool for investigating the water content and hydration profile of skin. The penetration depth into tissue (up to 1 mm) of TPI is comparable with optical coherence tomography and near-IR confocal microscopy and allows investigation of subsurface abnormalities. Through examination of the terahertz waveform in both the time and frequency domain [66], TPI may prove advantageous in distinguishing type, lateral spread, and depths of tumors prior to and during surgery.

A. Tissue Phantoms

Despite successful attempts to model the interaction of terahertz radiation with tissue, the models do not work when the tissue contains a high proportion of lipids, for example, as found in breast tissue. More complex models are needed, but prior to that a better understanding of the interaction of terahertz with the main constituents of tissue is required. The TPI data of tissue does not lend itself well to 3-D imaging due to the high absorption and matched refractive indices of tissue layers at terahertz frequencies, thus it is difficult to separate structure from absorption information. Further understanding of the source of contrast in terahertz images of tissue and correlation with other imaging modalities such as MRI and OCT is required to develop models to produce absorption profiles and structural data from TPI data. With that aim in mind Reid *et al.* [67] developed a tissue phantom for use at terahertz frequencies. Tissue-mimicking phantoms for the terahertz regime were developed to aid the current understanding of contrast mechanisms of tissue with TPI.

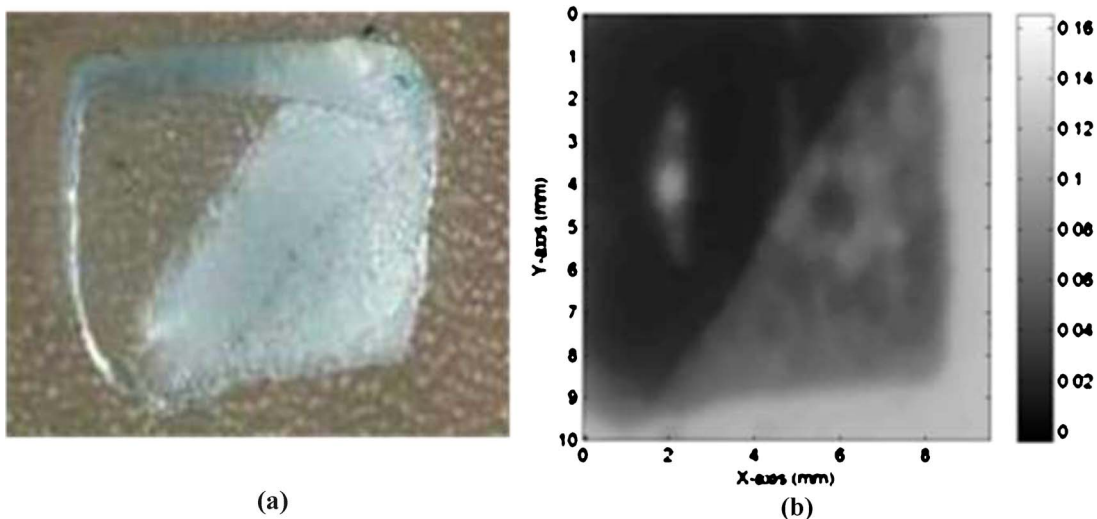


Fig. 12. (Color online) (a) Photographic image of a graduated tissue phantom and (b) 2-D terahertz image of the same phantom.

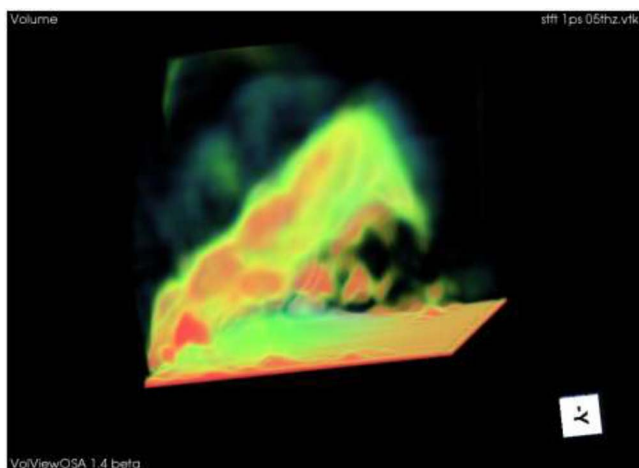


Fig. 13. (Color online) Three-dimensional image of a two-layered tissue phantom (View 7). The flat bottom surface is clearly seen and the angled green/red region is the interface between the two different phantoms.

The phantoms, comprising mixtures of water and protein, mimic biological tissue in both the spatial and the spectroscopic regimes. Terahertz spectroscopy of the individual phantom constituents has been performed with reflection measurements of phantoms of varying compositions [68]. Phantom composition was varied enabling the emulation of specific tissue properties, thus allowing the analysis of parameters such as the error with which discrete components can be identified: 7.5% for low gelatin concentration gels and 17% for higher concentration gels. Identifying this uncertainty is important when imaging tissues that have surface features not obvious to other techniques such as imaging of dysplasia. Figures 12(a) and 12(b) show the photographic image and terahertz image of a graduated tissue phantom, respectively, which was scanned with the Imaga1000. The terahertz image in Fig. 12(b) shows the maximum of the reflected pulse normalized by the minimum of the reflected pulse. The graduated phantom comprises two different phantom materials; the first, seen in the lower right-hand side of Fig. 12(a), is a 10% gelatin in water gel, and the second is a 40% gelatin in water gel. Figure 12(b) highlights the pro-

nounced difference in reflected signal from materials of differing water composition. Figure 13 shows the 3-D dataset of the graduated tissue phantom orthogonal to the orientation shown in Fig. 12(b). The 3-D dataset extends to 2 mm into the phantom and displays good contrast resolution distinguishing the two phantom materials at depth through the graduated phantom. Further studies under various conditions will allow us to determine the limits of detection and will lead to revised models of the interaction of terahertz radiation with biological tissues.

B. Tissue Scaffolds

A number of different methods have been described in the literature for preparing porous structures to be employed as tissue engineering scaffolds. Tissue scaffolds are integral to many regenerative medicine therapies, providing suitable environments for new tissue to grow. To assess their suitability, methods to routinely and reproducibly characterize scaffolds are needed [69]. Characterization of scaffolds is difficult due to their complex structure; they are hard spongelike material, predominantly made from a polymer framework with air gaps or pores. Depending on the method of manufacture and production variables, the size and density of the pores can vary significantly. A recent paper by Mather *et al.* [69] surveyed different imaging modalities and analysis techniques used to characterize scaffolds fabricated from poly(lactic-co-glycolic acid) using supercritical carbon dioxide. Three structurally different scaffolds were imaged using scanning electron microscopy, micro x ray, computed tomography, magnetic resonance imaging, and TPI. In each case two-dimensional images were obtained, from which scaffold properties were determined using image processing. The findings of this work highlight how the chosen imaging modality and image-processing technique can influence the results of scaffold characterization. It is concluded that to obtain useful results from image-based scaffold characterization, an imaging methodology providing sufficient contrast and resolution must be used along with robust image segmentation methods to allow intercomparison of results [69].

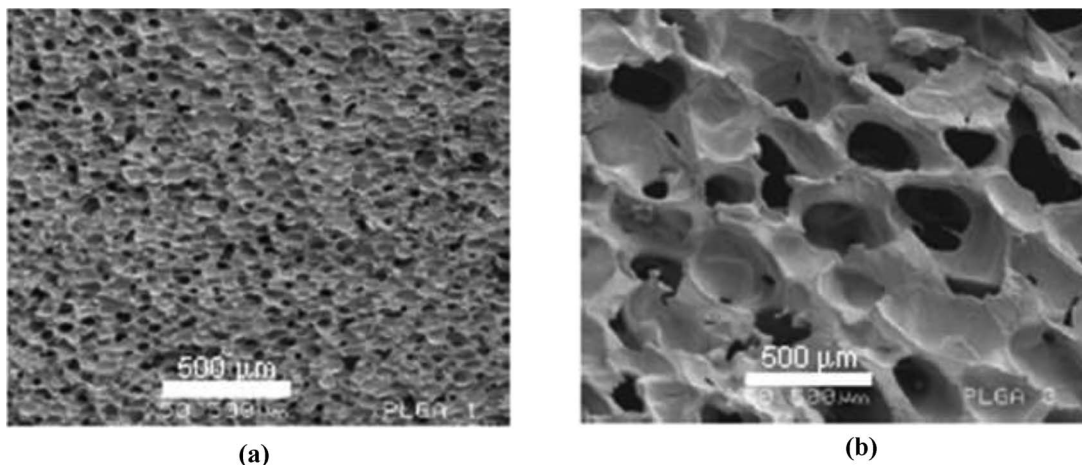


Fig. 14. (a) Scanning electron microscopy (SEM) of a scaffold with 50 μm average pore size and (b) SEM of a scaffold with an average pore size of 320 μm .

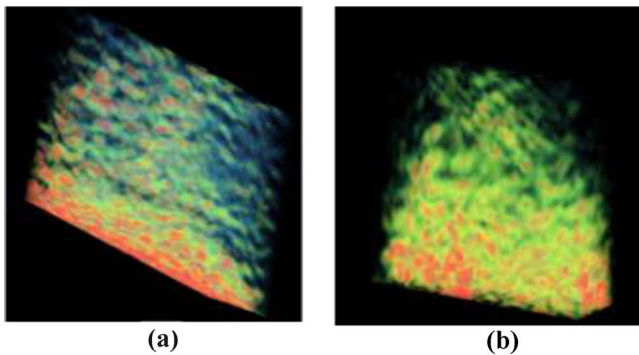


Fig. 15. (Color online) Three-dimensional terahertz images of tissue scaffolds with (a) 50 μm and (b) 320 μm average pore size (View 8).

Truly 3-D imaging techniques, such as TPI, may be advantageous for the characterization of scaffold material. TPI images were obtained without any sample preparation and provided good contrast between the porous and polymer phases. The main disadvantage of this approach is the low lateral resolution. Although terahertz radiation is not as penetrating as x rays, some useful depth information can be obtained. Here we present the TPI data acquired with the Imaga1000. We focus on two scaffolds with a pore size determined to be 50 and 320 μm from electron micrographs (see Fig. 14); both scaffolds were approximately 10 mm in diameter and between 5 and 10 mm in height. These samples were imaged without the quartz window in place in the Imaga1000, and the beam was focused approximately 1 mm into the scaffolds ($t = 1.5$ ps and $f = 1.5$ THz). The 3-D datasets were processed using STFT with the time and frequency settings the same for both scaffolds; the 3-D views are presented in Fig. 15. The differences in pore size can be clearly seen between Figs. 15(a) and 15(b). Given that the mean wavelength of the terahertz radiation at 1.5 THz is approximately 500 μm , we would expect the scattering to be more isotropic for the smaller pores and more anisotropic for the larger pores and the scattering coefficient to be approximately 100 times larger [70]. This is confirmed in the images; more radiation is detected from deeper within the scaffold with the smaller pores [Fig. 15(a)] than from the one with the larger pores [Fig. 15(b)]. Although the complex nature of these scaffolds combined with the resolution of terahertz imaging may not allow for direct determination of the structure and pore size, it may be possible to determine average scatter size, which is directly related to the scaffold's physical properties [71].

8. CONCLUSIONS

There have been significant advances in terahertz imaging over the past 10 years. Today, portable terahertz imaging systems and spectrometers are commercially available and are being applied to a wide range of problems. Data collection times are now down from hours to minutes, albeit over moderately sized areas. As faster delay line technology has been developed, line scans (b-scans) can be performed in seconds with advanced beam scanning techniques. With the advances in publishing we have presented terahertz data in 3-D for the first time using in-

teractive publishing tools. We have provided examples from a number of application areas ranging from quality control, security screening, pharmaceutical analysis, and biomedical applications. Although these are just a subset, they powerfully demonstrate the potential of terahertz imaging in a number of niche applications. However, there are still a number of hurdles that need to be overcome. Time-domain imaging is unique in that it has the potential to provide structural and chemical information for identification but requires expensive laser systems and equipment. A number of technical advances in laser, semiconductor, and scanning techniques are required to take some of the applications from the laboratory into the mainstream. Additionally, understanding the nature of the interaction of terahertz radiation with complex molecules, proteins, cells, and tissue remains a challenge. However, with real-time imaging and detector arrays on the horizon, terahertz imaging has a bright future.

ACKNOWLEDGMENTS

We thank S. Y. Huang from the Chinese University of Hong Kong for Fig. 1, TeraView Ltd. for the use of their data to produce Fig. 6, and M. Mather from the University of Nottingham for the scanning electron microscope images in Fig. 14.

REFERENCES

1. D. Abbott and X. C. Zhang, "Special issue on T-ray imaging, sensing, and detection," *Proc. IEEE* **95**, 1509–1513 (2007).
2. P. H. Siegel, "Terahertz technology," *IEEE Trans. Microwave Theory Tech.* **50**, 910–928 (2002).
3. H. Reubens and E. F. Nichols, "Heat rays of great wave length," *Phys. Rev.* **4**, 314–323 (1897).
4. E. F. Nichols, "A method for energy measurements in the infra-red spectrum and the properties of the ordinary ray in quartz for waves of great wave length," *Phys. Rev.* **4**, 297–313 (1897).
5. D. H. Auston, "Picosecond optoelectronics switching and gating in silicon," *Appl. Phys. Lett.* **26**, 101–103 (1975).
6. D. Grischkowsky, S. Keiding, M. Vanexter, and C. Fattinger, "Far-infrared time-domain spectroscopy with terahertz beams of dielectrics and semiconductors," *J. Opt. Soc. Am. B* **7**, 2006–2015 (1990).
7. R. A. Cheville and D. Grischkowsky, "Time-domain terahertz impulse ranging studies," *Appl. Phys. Lett.* **67**, 1960–1962 (1995).
8. B. B. Hu and M. C. Nuss, "Imaging with terahertz waves," *Opt. Lett.* **20**, 1716–1718 (1995).
9. D. M. Mittleman, R. H. Jacobsen, and M. C. Nuss, "T-ray imaging," *IEEE J. Sel. Top. Quantum Electron.* **2**, 679–692 (1996).
10. H. Harde and D. Grischkowsky, "Time-domain spectroscopy of molecular vapors with subpicosecond pulses of THz radiation," *Inst. Phys. Conf. Ser. (126)*, 217–222 (1992).
11. W. L. Chan, J. Deibel, and D. M. Mittleman, "Imaging with terahertz radiation," *Rep. Prog. Phys.* **70**, 1325–1379 (2007).
12. M. Nagel, F. Richter, P. Haring-Bolivar, and H. Kurz, "A functionalized THz sensor for marker-free DNA analysis," *Phys. Med. Biol.* **48**, 3625–3636 (2003).
13. P. H. Bolivar, M. Nagel, F. Richter, M. Brucherseifer, H. Kurz, A. Bossert-Hoff, and R. Buttner, "Label-free THz sensing of genetic sequences: towards THz biophysics," *Philos. Trans. R. Soc. London, Ser. A* **362**, 323–333 (2004).
14. D. F. Plusquellic, K. Siegrist, E. J. Heilweil, and M. Esenturk, "Applications of terahertz spectroscopy in

- biosystems," *ChemPhysChem* **8**, 2412–2431 (2007).
15. M. C. Kemp, "Detecting hidden objects: security imaging using millimetre-waves and terahertz," in *IEEE Conference on Advanced Video and Signal Based Surveillance* (IEEE, 2007), pp. 7–9.
 16. J. A. Zeitler, P. F. Taday, D. A. Newnham, M. Pepper, K. C. Gordon, and T. Rades, "Terahertz pulsed spectroscopy and imaging in the pharmaceutical setting—a review," *J. Pharm. Pharmacol.* **59**, 209–223 (2007).
 17. P. H. Siegel, "Terahertz technology in biology and medicine," *IEEE Trans. Microwave Theory Tech.* **52**, 2438–2447 (2004).
 18. E. Pickwell and V. P. Wallace, "Biomedical applications of terahertz technology," *J. Phys. D* **39**, R301–R310 (2006).
 19. J. A. Zeitler, P. F. Taday, K. C. Gordon, M. Pepper, and T. Rades, "Solid-state transition mechanism in carbamazepine polymorphs by time-resolved terahertz spectroscopy," *ChemPhysChem* **8**, 1924–1927 (2007).
 20. V. P. Wallace, P. F. Taday, A. J. Fitzgerald, R. M. Woodward, J. Cluff, R. J. Pye, and D. D. Arnone, "Terahertz pulsed imaging and spectroscopy for biomedical and pharmaceutical applications," *Faraday Discuss.* **126**, 255–263 (2004).
 21. J. A. Zeitler, D. A. Newnham, P. F. Taday, T. L. Threlfall, R. W. Lancaster, R. W. Berg, C. J. Strachan, M. Pepper, K. C. Gordon, and T. Rades, "Characterization of temperature-induced phase transitions in five polymorphic forms of sulfathiazole by terahertz pulsed spectroscopy and differential scanning calorimetry," *J. Pharm. Sci.* **95**, 2486–2498 (2006).
 22. J. A. Zeitler, P. F. Taday, M. Pepper, and T. Rades, "Relaxation and crystallization of amorphous carbamazepine studied by terahertz pulsed spectroscopy," *J. Pharm. Sci.* **96**, 2703–2709 (2007).
 23. M. Walther, B. M. Fischer, and P. U. Jepsen, "Noncovalent intermolecular forces in polycrystalline and amorphous saccharides in the far infrared," *Chem. Phys.* **288**, 261–268 (2003).
 24. S. Ebbinghaus, S. J. Kim, M. Heyden, X. Yu, U. Heugen, M. Gruebele, D. M. Leitner, and M. Havenith, "An extended dynamical hydration shell around proteins," *Proc. Natl. Acad. Sci. U.S.A.* **104**, 20749–20752 (2007).
 25. J. Xu, K. W. Plaxco, and S. J. Allen, "Probing the collective vibrational dynamics of a protein in liquid water by terahertz absorption spectroscopy," *Protein Sci.* **15**, 1175–1181 (2006).
 26. Q. L. Zhou, C. L. Zhang, K. J. Mu, B. Jin, L. L. Zhang, W. W. Li, and R. S. Feng, "Optical property and spectroscopy studies on the explosive 2,4,6-trinitro-1,3,5-trihydroxybenzene in the terahertz range," *Appl. Phys. Lett.* **92**, 101106 (2008).
 27. Y. C. Shen, P. F. Taday, and N. C. Kemp, "Terahertz spectroscopy of explosive materials," *Proc. SPIE* **5619**, 82–89 (2004).
 28. Y. C. Shen, T. Lo, P. F. Taday, B. E. Cole, W. R. Tribe, and M. C. Kemp, "Detection and identification of explosives using terahertz pulsed spectroscopic imaging," *Appl. Phys. Lett.* **86**, 1–3 (2005).
 29. Z. P. Jiang, F. G. Sun, and X. C. Zhang, "Terahertz pulse measurement with an optical streak camera," *Opt. Lett.* **24**, 1245–1247 (1999).
 30. D. M. Middleman, M. Gupta, R. Neelamani, R. G. Baraniuk, J. V. Rudd, and M. Koch, "Recent advances in terahertz imaging," *Appl. Phys. B* **68**, 1085–1094 (1999).
 31. J. A. Zeitler, Y. C. Shen, C. Baker, P. F. Taday, M. Pepper, and T. Rades, "Analysis of coating structures and interfaces in solid oral dosage forms by three dimensional terahertz pulsed imaging," *J. Pharm. Sci.* **96**, 330–340 (2007).
 32. V. P. Wallace, A. J. Fitzgerald, S. Shankar, N. Flanagan, R. Pye, J. Cluff, and D. D. Arnone, "Terahertz pulsed imaging of basal cell carcinoma ex vivo and in vivo," *Br. J. Dermatol.* **151**, 424–432 (2004).
 33. N. Katzenellenbogen and D. Grischkowsky, "Efficient generation of 380 fs pulses of THz radiation by ultrafast laser-pulse excitation of a biased metal-semiconductor interface," *Appl. Phys. Lett.* **58**, 222–224 (1991).
 34. Y. S. Jin, S. G. Jeon, G. J. Kim, J. I. Kim, and C. H. Shon, "Fast scanning of a pulsed terahertz signal using an oscillating optical delay line," *Rev. Sci. Instrum.* **78**, 023101–023105 (2007).
 35. G. J. Kim, S. G. Jeon, J. I. Kim, and Y. S. Jin, "Terahertz pulse detection using rotary optical delay line," *Jpn. J. Appl. Phys., Part 1* **46**, 7332–7335 (2007).
 36. R. M. Woodward, V. P. Wallace, R. J. Pye, B. E. Cole, D. D. Arnone, E. H. Linfield, and M. Pepper, "Terahertz pulse imaging of ex vivo basal cell carcinoma," *J. Invest. Dermatol.* **120**, 72–78 (2003).
 37. D. A. Crawley, C. Longbottom, B. E. Cole, C. M. Ciesla, D. Arnone, V. P. Wallace, and M. Pepper, "Terahertz pulse imaging: a pilot study of potential applications in dentistry," *Caries Res.* **37**, 352–359 (2003).
 38. R. M. Woodward, B. E. Cole, V. P. Wallace, R. J. Pye, D. D. Arnone, E. H. Linfield, and M. Pepper, "Terahertz pulse imaging in reflection geometry of human skin cancer and skin tissue," *Phys. Med. Biol.* **47**, 3853–3863 (2002).
 39. E. Pickwell, V. P. Wallace, B. E. Cole, S. Ali, C. Longbottom, R. J. M. Lynch, and M. Pepper, "A comparison of terahertz pulsed imaging with transmission microradiography for depth measurement of enamel demineralisation in vitro," *Caries Res.* **41**, 49–55 (2007).
 40. D. M. Middleman, S. Hunsche, L. Boivin, and M. C. Nuss, "T-ray tomography," *Opt. Lett.* **22**, 904–906 (1997).
 41. E. Berry, J. W. Handley, A. J. Fitzgerald, W. J. Merchant, R. D. Boyle, N. N. Zinov'ev, R. E. Miles, J. M. Chamberlain, and M. A. Smith, "Multispectral classification techniques for terahertz pulsed imaging: an example in histopathology," *Med. Eng. Phys.* **26**, 423–430 (2004).
 42. T. Löffler, T. Bauer, K. J. Siebert, H. G. Roskos, A. Fitzgerald, and S. Czasch, "Terahertz dark-field imaging of biomedical tissue," *Opt. Express* **9**, 616–621 (2001).
 43. B. Pradarutti, G. Matthaus, S. Riehemann, G. Notni, S. Nolte, and A. Tuneremann, "Advanced analysis concepts for terahertz time domain imaging," *Opt. Commun.* **279**, 248–254 (2007).
 44. E. Berry, R. D. Boyle, A. J. Fitzgerald, and J. W. Handley, "Time-frequency analysis in terahertz-pulsed imaging," in *Computer Vision Beyond the Visible Spectrum* (Springer, 2005), pp. 271–311.
 45. J. Handley, A. J. Fitzgerald, E. Berry, and R. D. Boyle, "The short time Fourier transform applied to terahertz pulsed imaging," *Med. Phys.* **30**, 1541–1541 (2003).
 46. J. W. Handley, A. J. Fitzgerald, E. Berry, and R. D. Boyle, "Distinguishing between materials in terahertz imaging using wide-band cross ambiguity functions," *Digit. Signal Process.* **14**, 99–111 (2004).
 47. X. X. Yin, B. W. H. Ng, B. Ferguson, S. P. Micken, and D. Abbott, "2-D wavelet segmentation in 3-D T-ray tomography," *IEEE Sens. J.* **7**, 342–343 (2007).
 48. M. C. Kemp, P. F. Taday, B. E. Cole, J. A. Cluff, A. J. Fitzgerald, and W. R. Tribe, "Security applications of terahertz technology," *Proc. SPIE* **5070**, 44–52 (2003).
 49. W. R. Tribe, D. A. Newnham, P. F. Taday, and M. C. Kemp, "Hidden object detection: security applications of terahertz technology," *Proc. SPIE* **5354**, 168–176 (2004).
 50. C. Baker, T. Lo, W. R. Tribe, B. E. Cole, M. K. Hogbin, and M. C. Kemp, "Detection of concealed explosives at a distance using terahertz technology," *Proc. IEEE* **95**, 1559–1565 (2007).
 51. Y. C. Shen and P. F. Taday, "Development and application of terahertz pulsed imaging for nondestructive inspection of pharmaceutical tablet," *IEEE J. Sel. Top. Quantum Electron.* **14**, 407–415 (2008).
 52. J. A. Zeitler and L. F. Gladden, "In-vitro tomography and non-destructive imaging at depth of pharmaceutical solid dosage forms," *Eur. J. Pharm. Biopharm.* (to be published).
 53. A. J. Fitzgerald, B. E. Cole, and P. F. Taday, "Nondestructive analysis of tablet coating thicknesses using terahertz pulsed imaging," *J. Pharm. Sci.* **94**, 177–183 (2005).
 54. Y. C. Shen, P. F. Taday, D. A. Newnham, and M. Pepper,

- “Chemical mapping using reflection terahertz pulsed imaging,” *Semicond. Sci. Technol.* **20**, S254–S257 (2005).
55. R. P. Cogdill, S. M. Short, R. Forcht, Z. Shi, Y. C. Shen, P. F. Taday, C. A. Anderson, and J. K. Drennen, “An efficient method-development strategy for quantitative chemical imaging using terahertz pulse spectroscopy,” *J. Pharm. Innovation* **1**, 63–75 (2006).
 56. Y. C. Shen, P. F. Taday, D. A. Newnham, M. C. Kemp, and M. Pepper, “3-D chemical mapping using terahertz pulsed imaging,” *Proc. SPIE* **5727**, 24–31 (2005).
 57. J. A. Spencer, Z. Gao, T. Moore, L. F. Buhse, P. F. Taday, D. A. Newnham, Y. Shen, A. Portieri, and A. Husain, “Delayed release tablet dissolution related to coating thickness by terahertz pulsed image mapping,” *J. Pharm. Sci.* **97**, 1543–1550 (2008).
 58. L. Ho, R. Mueller, K. C. Gordon, P. Kleinebudde, M. Pepper, T. Rades, Y. C. Shen, P. F. Taday, and J. A. Zeitler, “Applications of terahertz pulsed imaging to sustained-release tablet film coating quality assessment and dissolution performance,” *C. R. Math.* **127**, 79–87 (2008).
 59. R. Palermo, R. P. Cogdill, S. M. Short, J. K. Drennen III, and P. F. Taday, “Density mapping and chemical component calibration development of four-component compacts via terahertz pulsed imaging,” *J. Pharm. Biomed. Anal.* **46**, 36–44 (2008).
 60. J. Obradovic, J. H. P. Collins, O. Hirsch, M. D. Mantle, M. L. Johns, and L. F. Gladden, “The use of THz time-domain reflection measurements to investigate solvent diffusion in polymers,” *Polymer* **48**, 3494–3503 (2007).
 61. A. J. Fitzgerald, V. P. Wallace, M. Jimenez-Linan, L. Bobrow, R. J. Pye, A. D. Purushotham, and D. D. Arnone, “Terahertz pulsed imaging of human breast tumors,” *Radiology* **239**, 533–540 (2006).
 62. V. P. Wallace, A. J. Fitzgerald, E. Pickwell, R. J. Pye, P. F. Taday, N. Flanagan, and T. Ha, “Terahertz pulsed spectroscopy of human basal cell carcinoma,” *Appl. Spectrosc.* **60**, 1127–1133 (2006).
 63. V. P. Wallace, E. MacPherson, A. J. Fitzgerald, T. Lo, E. Provenzano, S. Pinder, and A. Purushotham, “Terahertz pulsed imaging and spectroscopy of breast tumors,” *Proc. SPIE* **6386**, U183–U190 (2006).
 64. E. Pickwell, B. E. Cole, A. J. Fitzgerald, V. P. Wallace, and M. Pepper, “Simulation of terahertz pulse propagation in biological systems,” *Appl. Phys. Lett.* **84**, 2190–2192 (2004).
 65. E. Pickwell, A. J. Fitzgerald, B. E. Cole, P. F. Taday, R. J. Pye, T. Ha, M. Pepper, and V. P. Wallace, “Simulating the response of terahertz radiation to basal cell carcinoma using ex vivo spectroscopy measurements,” *J. Biomed. Opt.* **10**, 064021–064027 (2005).
 66. E. Pickwell-MacPherson, T. Lo, A. Fitzgerald, E. Provenzano, S. Pinder, A. Purushotham, and V. P. Wallace, “Application of finite difference time domain methods to terahertz spectroscopy measurements of breast cancer,” in *Microwave Symposium, 2007. IEEE/MTT-S International* (IEEE, 2007), pp. 1379–1381.
 67. C. Reid, A. P. Gibson, J. C. Hebden, and V. P. Wallace, “An oil and water emulsion phantom for biomedical terahertz spectroscopy,” in *4th IEEE/EMBS International Summer School and Symposium on Medical Devices and Biosensors* (IEEE, 2007), pp. 4–7.
 68. C. Reid, A. P. Gibson, J. C. Hebden, and V. P. Wallace, “The use of tissue mimicking phantoms in analysing contrast in THz pulsed imaging of biological tissue,” in *Conference Digest of the Joint 32nd International Conference on Infrared and Millimetre Waves, and 15th International Conference on Terahertz Electronics* (IEEE, 2007), pp. 567–568.
 69. M. L. Mather, S. P. Morgan, L. J. White, H. Tai, W. Kockenberger, S. M. Howdle, K. M. Shakesheff, and J. A. Crowe, “Image-based characterization of foamed polymeric tissue scaffolds,” *Biomed. Mater.* **3**, 1–11 (2008).
 70. S. Prahl, “Mie scattering calculation,” (2007), retrieved July 8, 2008, http://omlc.ogi.edu/calc/mie_calc.html.
 71. K. Tahir and C. Dainty, “Experimental measurements of light scattering from samples with specified optical properties,” *J. Opt. A, Pure Appl. Opt.* **7**, 207–214 (2005).